



## **Aerodynamic Characterization of a Hooded Fairing Accommodating Winged Payloads**

*João F. A. Martos<sup>1</sup>, Johan Steelant<sup>1</sup>, Rafael O. Santos<sup>2</sup>, Marco A. S. Minucc<sup>2</sup>, Israel S. Rego<sup>2</sup>, Norton D. V. Assis<sup>2</sup>, Jefte S. Guimarães<sup>2</sup>, Amós G. Silva<sup>2</sup>, Pedro A. S. Matos<sup>2</sup>, Matheus T. A. Silva, Lucas A. G. Ribeiro, and Lucas G.*

### **Abstract**

For various high-speed applications such as hypersonic cruise vehicles or re-usable stages for access to space, there is a growing demand to perform dedicated small-scale flight experiments. The maturity in the various disciplines and technologies has evolved quite substantially in the last decade and has grown past the inherent limitations of on-ground facilities. For the applications in mind, a high aerodynamic efficiency for cruise or gliding demands naturally for winged concepts and related control surfaces to generate respectively lift and controllability.

As a low-cost solution to experimentally flight test winged concepts to their flight test conditions, the use of sounding rockets has proven to be a reliable and efficient way. However, the mass and dimensions of the flight test vehicle are often limiting factors by the launcher capability, specifically the latter due to the available volume under the fairing. Already for small span vehicles, the fairing diameter limits the overall size of the vehicle. Rather than a hammerhead fairing, a hooded fairing is proposed here allowing the wing span to cross the fairing's periphery. Consequently, the fairing diameter accommodates the vehicle main body and the hoods cover the outer parts of the wing span exceeding the fairing diameter. This solution optimizes the internal fairing volume with a minimal impact on the overall performance. However, this comes with a higher complexity for the structural design of the fairing.

An extensive experimental and numerical aerodynamics analysis has been performed for the proposed hooded fairing and is presented in this work. This aero-thermal database should provide the necessary pressure and thermal loads for a preliminary thermos-structural design of this hooded fairing.

**Keywords:** *CFD, Hypersonic, Fairing, Shock tunnel, Winged payload*

### **Nomenclature**

AoA – Angle of Attack	HXI – High Speed Experimental Fly Vehicles - International
h – Heat transfer coefficient	M – Mach Number
$C_l$ – Lift force coefficient	Re – Reynolds Number
$C_d$ – Drag force coefficient	ST – Shock tunnel
$C_m$ – Moment coefficient	St – Stanton Number
$C_p$ – Coefficient of pressure	TC – Telecommand
CFD – Computational Fluid Dynamics	TM – Telecontrol
EFTV - Experimental Flight Test Vehicle	TRL – Technology Readiness Level
h – Heat transfer coefficient	TVC – Thrust Vector Control
IEAv – Institute for Advanced Studies	

<sup>1</sup> *ESA-ESTEC, Aerothermodynamics and Propulsion Analysis Section TEC-MPA, P.O. Box 299, Noordwijk, Netherlands, JoaoMartos@gmail.com, Johan.Steelant@esa.int*

<sup>2</sup> *Division of Aerothermodynamics and Hypersonics, Institute for Advanced Studies, São José dos Campos, SP, Brazil, rafael.santos@ieav.cta.br, sala@ieav.cta.br, israel.rego@ieav.cta.br, norton@ieav.cta.br, jefte@gmail.com, amos@ieav.cta.br, pedrosmatos@gmail.com, matheus.a@ieav.cta.br, lucasag@ieav.cta.br, galembeck@ieav.cta.br*



## 1. Introduction

The design of high-speed airbreathing vehicles are an ongoing challenge with the potential to cut significantly the cruise time in case of air transport or to provide cheaper and reusable access to space presently dominated by rockets. A lot of progress has been made in the last decade in high-speed aerodynamics and flight control, high-speed propulsion and high-temperature materials achieving viable vehicle concepts according to their needed aero-thermo-propulsive performance. Despite the progress made in numerical and ground-test of such vehicles, performing a test flight at hypersonic speed will be the only way and the ultimate proof to demonstrate the technical feasibility of these new promising concepts and provide the needed data for validation and verification [1].

In this frame, the international HEXAFLY-INT (HXI) project aims to test in free-flight a scaled model above Mach 7 followed by a gliding phase from Mach 7 downwards. In addition, this high-speed vehicle platform allows to verify several breakthrough technologies on-board such as guidance, materials, air-data system, thermal control and others.

A low-cost solution to accelerate such flight test vehicles to their respective flight test condition is the use of sounding rockets flying a ballistic trajectory and releasing the vehicle/payload at a prescribed altitude and speed. In the case of HXI, the Experimental Flight Test Vehicle (EFTV) will be launched on a sounding rocket (the Brazilian VBS-43 single-stage booster equipped with an 8-ton solid rocket motor) in a suborbital trajectory with fairing release during ascent at around 75 km and a payload release at an apogee of about 90 km. The EFTV aims demonstrating its high aerodynamic efficiency based upon a waverider design having a finite wing span and control surfaces to manoeuvrability and controllability. In those cases, not the vehicle mass but rather the wing span is predominantly the limiting factor, i.e. fitting within the available dimensions of the fairing. To circumvent this restriction, a hammerhead fairing is often proposed as a solution but has an important impact on the overall drag and payload performance. An alternative solution is to let the wing span cross the fairing's periphery. The protruded parts can then be thermally and aerodynamically protected by mounting customized hoods to the fairing. As such, the fairing diameter is optimally used to accommodate the vehicle main body whereas the hoods cover up the wings' tips and control surfaces. To assure a proper functioning of such a hooded fairing throughout the ascent of the sounding rocket, a dedicated experimental and numerical aerodynamics analysis is needed.

The main purpose of this work is the determination of aero-thermal and release loads to which the fairing will be subjected during flight. The detailed design, structural analysis and manufacturing of the fairing requires a complete aero-thermal load analysis considering the maximum loads during flight (transonic flight and highest dynamic pressure). In addition, for the fairing release above 75km altitude, it is necessary to prevent any interference or collision with the payload (vehicle), in particular for the CMC based ailerons an aerodynamics data-base will be generated numerically along the flight path along with an experimental validation at one particular point along the trajectory. Classically, blunted nose cone aerodynamics are well known and was used as reference guideline.

## 2. HXI Mission

The overall shape of the hooded fairing was defined by the HEXAFLY-INT mission which is a free-flight glider testing an innovative high-speed waverider with several breakthrough technologies on board. This approach will create the basis to gradually increase the TRL level relevant to the design of hypersonic vehicles. The EFTV is conceived to achieve a level flight at an altitude of about 32 km, after a pull-out manoeuvre during the descent of a suppressed trajectory [2]. However, for the preliminary design of the fairing, only the ascending part of the ballistic flight is of interest until fairing release. The VBS-43 Launch Vehicle lifts off in vertical position from a launch stool in CLA (Alcântara Launch Center - Brazil). A pitch-over manoeuvre induces a suppressed trajectory. The VBS-43 burns out at 65s which is below 40km altitude and the fairing release shall be above 75km altitude by pushing it off forward. After the release from the launcher, the payload consists of two main parts, the Experimental Flight Test Vehicle (EFTV) and the Experiment Support Module (ESM) (Fig. 1).

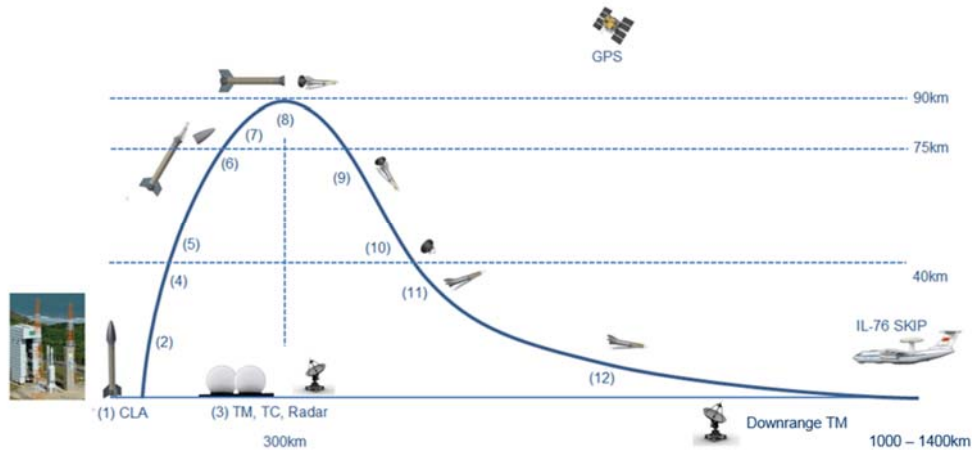


**Fig. 1:** HXI mission profile.

1. The VBS-43 Launch Vehicle lifts off in vertical position from a launch stool in CLA (Alcântara).
2. A pitch over manoeuvre induces the suppressed trajectory. The TVC corrects for any disturbances during propelled flight.
3. Ground stations, located on the Launch Range, track the flight (Radar, GPS), receive data from (TM), and send data to (TC) the Launch Vehicle.
4. The VBS-43 burns out at 65s which is below 40km.
5. In the jet-off flight phase, fins passively stabilize the vehicle and an active Cold Gas System provides rate and attitude control at high altitude.
6. Fairing release shall be above 75km.
7. Attitude stabilization of launch vehicle is required prior to Payload release.
8. Payload release is foreseen in a horizontal flight path angle at around 90km apogee.
9. Cruise phase to the experiment window. Stabilization and coarse attitude control are achieved with a Cold Gas System.
10. ESM separation from the EFTV at around 40km.
11. Pull-out manoeuvre.
12. Experiment window; Glider (EFTV) manoeuvres until touch down. The data reception along the flight path is secured with a downrange TM station.

### 3. Experimental Test Set-Up

#### 3.1. Test Facility and Model

The hypersonic tunnel T2 of IEAv (Fig. 2) consists of a high pressure 1.8 m long driver cylindrical tube connected to a 6.4 m low pressure driven, separated by a Double-Diaphragm Section (DDS), which is in general filled with Argon or Helium and is used to have a more precise control of the main copper diaphragms rupture. At the end of the driven section, there is a secondary aluminium diaphragm that prevents the test gas to flow into the test section before the experiment actually begins. The test section has a cylindrical shape of 60 cm length and 40 cm internal diameter and is connected to a 2 m<sup>3</sup> dump tank. The total length of the T2 hypersonic tunnel is about 12 meters. Although the tunnel has been designed to operate up to a maximum pressure of 23.0 MPa, for safety reasons the pressure in the driver has been set to 3000 psi (about 20 MPa) for all runs [3]. The T2 tunnel is capable of generating low, medium and high enthalpy hypersonic flow conditions at different Mach number. For the present investigations, only medium enthalpy operation modes were considered, where a steady flow duration (useful test time) of some milliseconds and freestream Mach number ranging from 7 to 8 could be produced. High enthalpy runs did not yield suitable freestream conditions associated to the HXI fairing flight.

In order to represent the flight conditions properly, the experimental set-up must match flow similarities such as Mach and Reynolds number considering the test section area available and the preliminary design of the flight model, therefore the experimental model was designed at 1:14.4 scale (**Fig. 3a**).

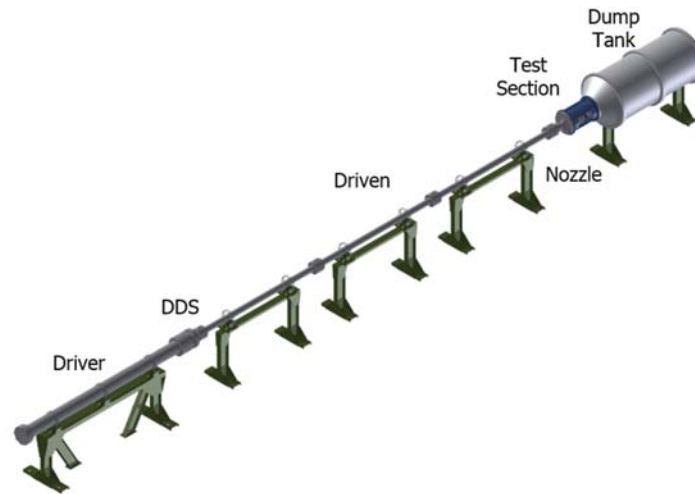


**Fig. 2:** The T2 Hypersonic Shock Tunnel

Since the final design of the fairing is open, the model should be as flexible and easy for adaptations as possible by making use of 3-D prototyping techniques. The main goal was to achieve a good trade-off between mass, production time and mechanical strength. To do so, the blunt nose was made out of metal to withstand the heat transfer and the main body made out of printed polymer (Fig. 3 b). The feasibility study of utilization of 3-D Printing technology on hypersonic test models has already been done at IEAv [4]. To facilitate the instrumentation installation, the main body was divided in two pieces connected by the steel nose and a sword in its back. The body was designed to improve the surface quality according to the printing direction and to accommodate the sensors. Sensors were distributed in opposite lines to measure the hoods effects. Also, in order to simulate all flight conditions accordingly, a new model support was designed to operate between  $-9^\circ$  and  $9^\circ$  with steps of  $1^\circ$  angle of attack (AoA) and maintain the test model in the centreline of the nozzle (Fig. 3b).

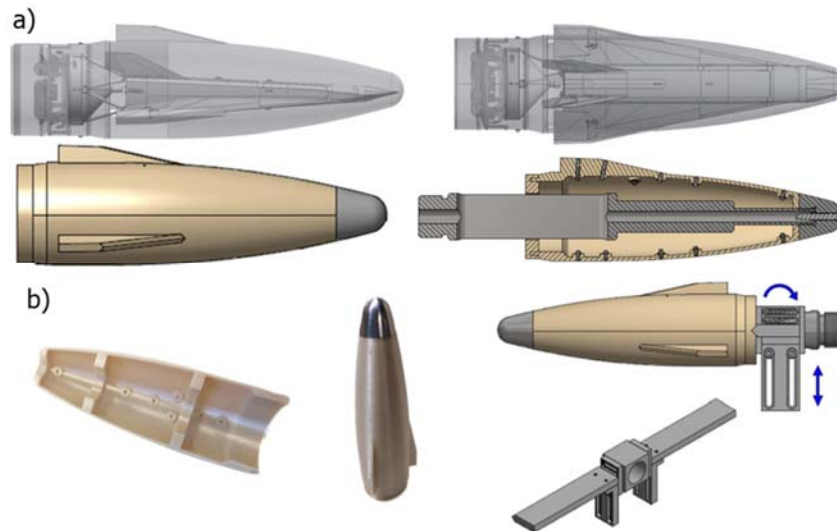


**Fig. 3:** Flight and experimental model; b) Hybrid printed model and AoA support

**Fig. 4** shows the model fitted inside the test section with the newly manufactured fastening bracket, designed to allow the model to be tilted at different angles of attack (AoA). Classical measurements as pressure transducer and high-speed schlieren visualization were employed to obtain respectively wall pressure and flowfield characteristics over the HXI fairing at hypervelocity. Because of the small sub-scale of the model, the use of tiny pressure sensors was mandatory (Fig. 5). The rigid metallic sting showed however high mechanical vibration modes, which, when coupled to the plastic model, led to

fluctuations of the signal measured by each sensor on it. The best solutions found to reduce this mechanical vibration noise were: mechanical isolation of the fastening bracket from the plastic model through a thin rubber ring at the rear end of the model, production of a high enthalpy reservoir of test gas (due to the fact that the impulse transferred to the nozzle entrance is much lower in the high enthalpy runs [13]), and flush installation of the surface pressure sensors fixed with the help of sealing rings (Fig. 6). In addition, the data acquisition solutions and post-analysis techniques were applied together to mitigate any possible mechanical vibration interference in the measured values of pressure.

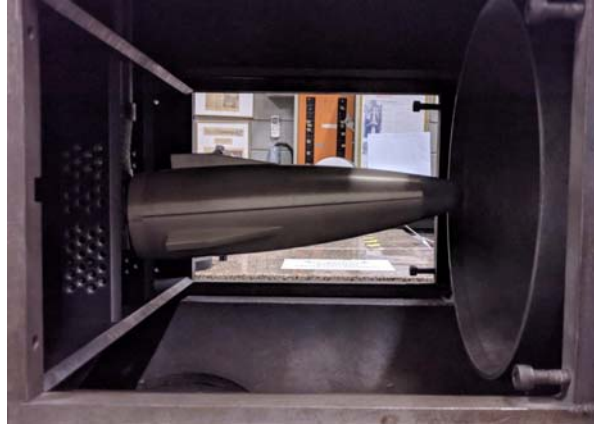


**Fig. 4:** HXI sub-scale fairing model fixed to the fastening bracket installed into the T2 test section.

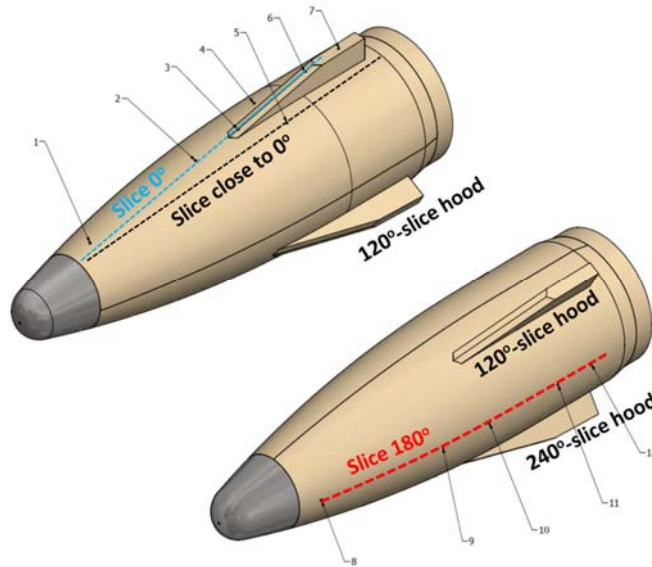


**Fig. 5:** Pressure sensor tags over slices of the HXI fairing sub-scaled model.

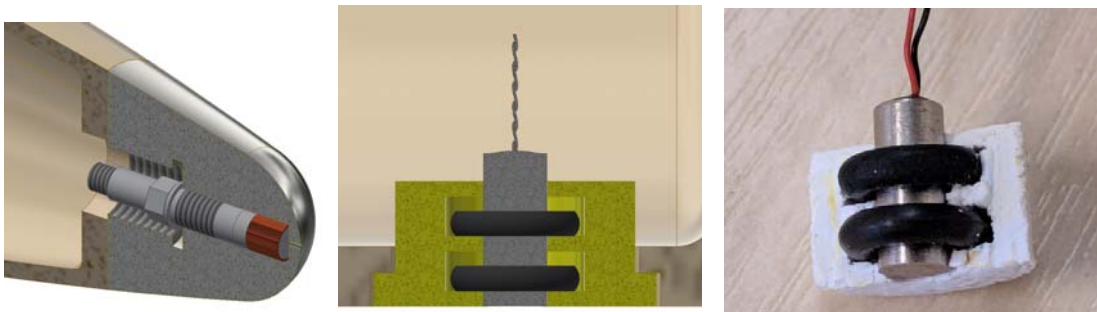


**Fig. 6:** Pitot probe (recessed installation) and surface pressure sensors (flush installation).

### 3.2. Experimental conditions

The main purpose of the campaign was to validate ESA computational simulations of the HXI fairing. To reproduce the expected flow properties encountered during ascent, the freestream flow properties should be set to match the Reynolds and Mach number considering the scale based on the  $\rho L$  correlation by keeping the same temperature and adjusting the pressure. According to T2 capability and considering  $\rho L$  scaling, a flight point around  $\sim 44.38$  km, Mach 7.32 and Reynolds number  $3.3E+05$  was chosen since the obtained flow conditions represent Mach and Reynolds Number at conditions used before in the T2 tunnel. The map of operability for the T2 tunnel is presented in Fig. 7, where the grey area presents the tunnel capability only in terms of pressure while the blue represents the tunnel capability in terms of Reynolds similarity considering scaling along with the trajectory of VS-43 [2, 3].

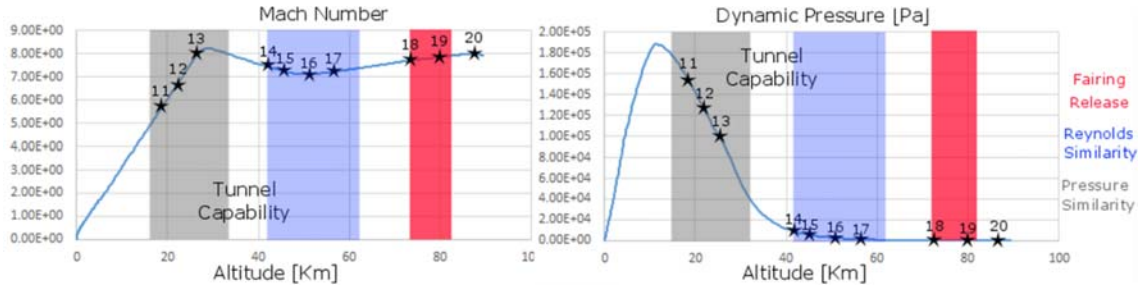


**Fig. 7:** Tunnel capability considering pressure (grey) and Reynolds (blue) similarity and flight-test conditions.

The T2 operational set-up which reproduced at best the HXI fairing freestream conditions, were: Helium gas at 3,000 psi in the driver section, air as test gas at 1 atm in the driven section, and an area ratio for the convergent-divergent nozzle of 225. Only 16 of 32 runs under such operational set-up were successfully performed, as listed in Table 1.

**Table 1: Reservoir and Freestream conditions and model AoA for successful runs**

#Run	Reservoir conditions		Freestream conditions		AoA [degree]
	$P_0$ [MPa]	$T_0$ [K]	$Re_\infty$	$M_\infty$	
13	10,22	1946	$3,4E+05$	8,13	0,0
14	12,77	2213	$3,2E+05$	7,58	0,0
15	11,49	2081	$3,4E+05$	7,58	5,0
16	11,55	2088	$3,3E+05$	7,59	9,0
17	11,49	2081	$1,2E+04$	4,97	9,0
18	11,25	2056	$3,4E+05$	7,63	6,0
20	10,99	2029	$3,5E+05$	7,57	3,0
21	12,77	2213	$3,0E+05$	7,67	3,0
23	10,83	2012	$2,8E+05$	7,74	6,0
24	12,01	2136	$3,3E+05$	7,61	6,0
25	11,49	2081	$3,3E+05$	7,62	9,0
27	11,91	2125	$3,3E+05$	7,67	-9,0
28	12,27	2162	$3,3E+05$	7,68	-9,0
29	12,12	2147	$3,3E+05$	7,61	-6,0
30	12,38	2174	$3,2E+05$	7,62	-6,0
31	11,49	2081	$3,3E+05$	7,63	-3,0
32	11,66	2099	$3,4E+05$	7,60	-3,0

#### 4. Numerical Approach and Simulations

The hypersonic shock tunnel T2 utilizes a conical nozzle to expand and accelerate the flow to the desired test conditions. However, the flow divergence should be analysed for any comparison between numerical and experimental results since the exit flow is not uniform. In order to simulate the nozzle divergence, a set of CFD simulations purely for the nozzle were performed and these results are used as boundary conditions for the experimental model simulation composed of a cylindrical domain for reasons of compatibility (Fig. 8). For the nozzle simulation a two-dimensional mesh was generated and transformed into a slice with  $1^\circ$  width, a two-dimensional approach was used since no swirl or 3D effects are expected. The 2D mesh was generated in CENTAUR and transformed into an axisymmetric slice for resolution with TAU. The computational domain comprised approximately half million nodes including a prismatic layer consisted of 75 elements with first cell height of  $5 \mu\text{m}$ . The shock tube stagnation pressure and density were imposed as inlet conditions, whereas the vacuum pressure achieved in the dump tank was prescribed as outlet condition to the numerical domain.

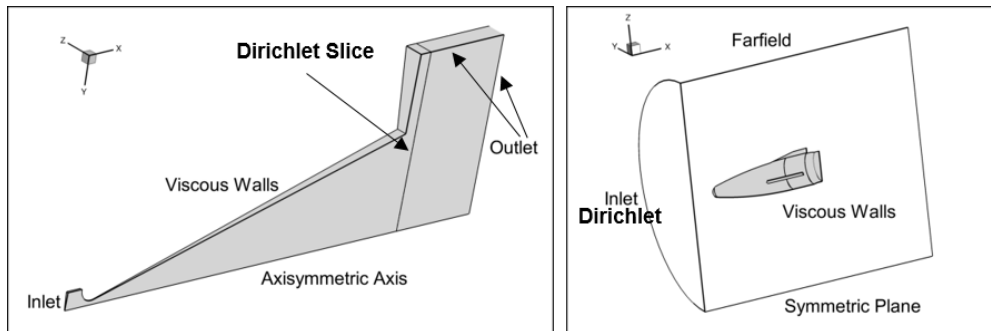


**Fig. 8:** CFD domain for Nozzle, Blunted Cone and Experimental Model.

As stated before a cylindrical domain was used to simulate the nozzle exit conditions imposed at experimental model simulations varying between uniform flow (expected experimental freestream flow properties) and inlet that uses the nozzle exit simulation as input (Dirichlet shown in Fig. 8). The simulations for the experimental model were based on a hybrid grid generated in Centaur of 1.2 to 3.6 million nodes (4 to 12.6 million elements) depending on model configuration (without or with the hoods respectively). A prismatic layer consisted of structured-squared grid was used in the surface to optimize the heat flux estimation over the surface. The prismatic extrusion comprised 100 cells with increasing height from the wall at a stretching ratio of 1.05 after the first 10 cells with uniform height of  $10 \mu\text{m}$  to obtain a  $Y^+$  lower than 1. For example, Fig. 9 shows an overview of the surface and prismatic meshes (on the left), with detail of the mesh (on the right).

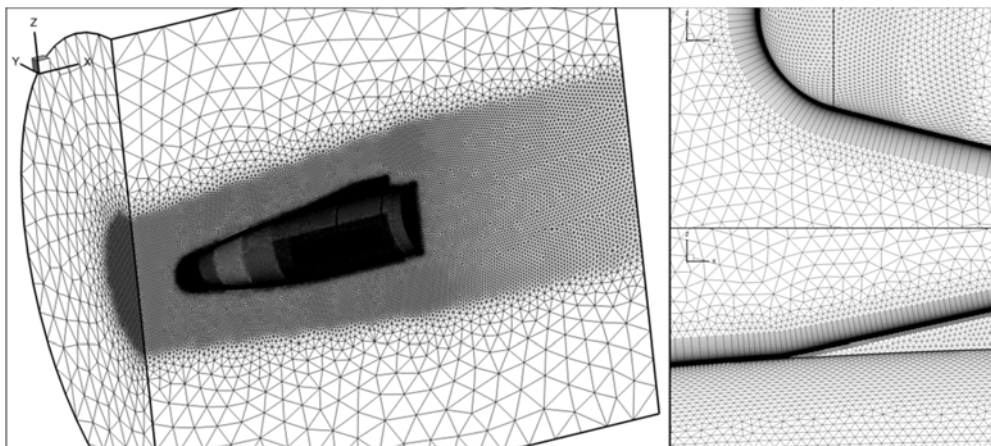


**Fig. 9:** Mesh for the experimental model simulations and details of prismatic layer over the nose and top hood.

The flow field was resolved with the code TAU [5], discretizing the fluxes in the Navier-Stokes equations and the eddy viscosity model accordingly to the upwind second-order AUSMDV scheme [6]. The

turbulence model used was Spalart-Allmaras model with a freestream turbulent intensity of 0.1% [7]. A least-square reconstruction of the gradients was used, which proves to be more accurate than the Green-Gauss approach in case of hybrid grids [8]. Finally, the RANS equations were integrated towards the steady solution by means of a backward Euler time-relaxation scheme [9].

#### 4.1. Blunted Cone Validation

Theoretical-analytical formulations developed for laminar and turbulent flow skin friction on a sharp cone were used to validate the numerical set-up in terms of mesh resolution and solver settings (numerical scheme...) on a blunted cone without hoods. As skin friction values are sensitive to the simulation accuracy of the boundary layer, they can be used as a figure of merit and used as a validation benchmark using well-known skin friction correlations for flat plates and cones. Corrections accounting for compressible flow were applied. Based on law of the wall theory applied to compressible flows, the skin friction is calculated for a Blasius' laminar flow while the Van Driest theory was used to calculate the skin friction for turbulent flow (Fig. 10) [10].

Skin friction coefficient

$$c_f = \frac{\tau_w}{\frac{1}{2}\rho_\infty u_\infty^2} \quad (1)$$

Laminar skin friction coefficient for compressible flow

$$c_{f,plate} = \frac{0.667 \cdot \sqrt{C_w}}{\sqrt{Re_x}} \text{ with } C_w = \frac{\rho_w \mu_w}{\rho_e \mu_e}; c_{f,cone} = c_{f,plate} \cdot \sqrt{3} \quad (2)$$

Turbulent skin friction coefficient for compressible Flow

$$c_{f,plate} = \frac{0.455}{S^2 \left[ \ln\left(\frac{0.06}{S^2} Re_{x,i} \frac{\mu_e}{\mu_w} \sqrt{\frac{T_e}{T_w}}\right) \right]^2}; c_{f,cone} = c_{f,plate} \cdot 1.141 \quad (3)$$

$$S = \frac{(T_{aw}/T_e - 1)^{1/2}}{\sin^{-1} A + \sin B}; A = \frac{2a^2 - b}{(b^2 + 4a^2)^{1/2}} \text{ and } B = \frac{b}{(b^2 + 4a^2)^{1/2}}; a = \left(\frac{\gamma - 1}{2} M_e^2 \frac{T_e}{T_2}\right)^{1/2} \text{ and } b = \left(\frac{T_{aw}}{T_w} - 1\right) \quad (3.1)$$

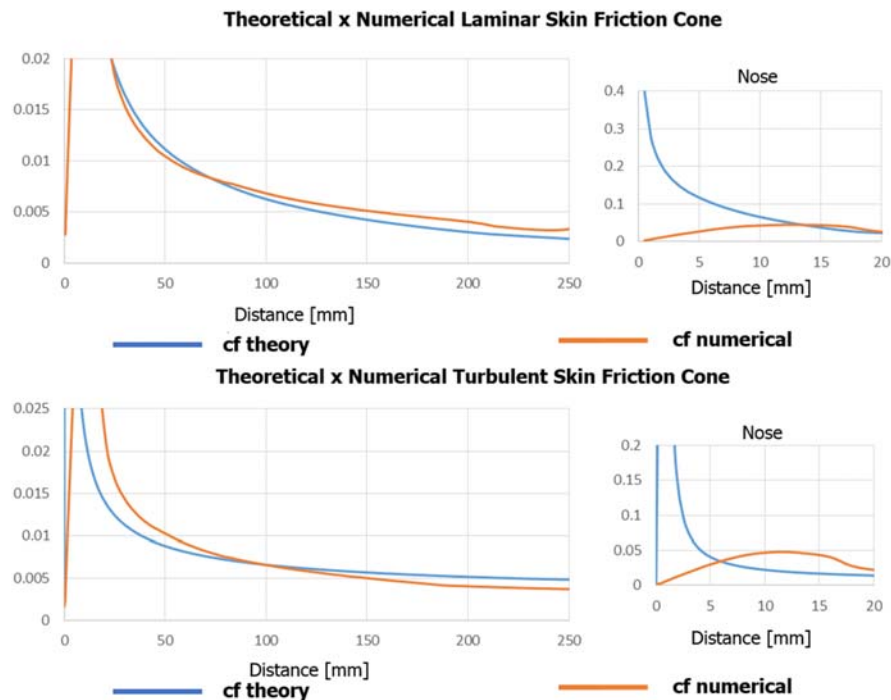


**Fig. 10:** Theoretical and numerical skin friction coefficient over a cone for laminar (top) and turbulent (bottom).

The cone tip and downstream curvature were considered for the distance travelled over the surface to calculate the  $Re_x$ . The edge flow properties were the properties between the boundary layer and the shock wave considering uniform freestream. The discrepancy is higher closer to the nose due to higher gradients in the stagnation point. Downstream of the blunted nose, the agreement obtained between flat plate/perfect cone theory and simulations are very good and well below the numerical errors embedded in those theoretical correlations. As such the results are considered representative to validate the numerical set-up as the Van driest theory has an estimate error of 8% [10] and the maximum difference obtained was 5%.

**4.2. Nozzle simulation**

Divergence and non-uniform flow are results of a conical nozzle, despite for its advantages in terms of versatility in Mach number it presents these disadvantages at nozzle exit. Temperature, pressure and velocity changes according to Y coordinate and it should be considered for the experimental validation. Fig. 11 shows the numerical set-up used for T2 nozzle simulations considering that the flow is two dimensional and expected flow properties [Total Pressure =  $1.283 \cdot 10^{+7}$  Pa and Total Temperature = 3075 K].

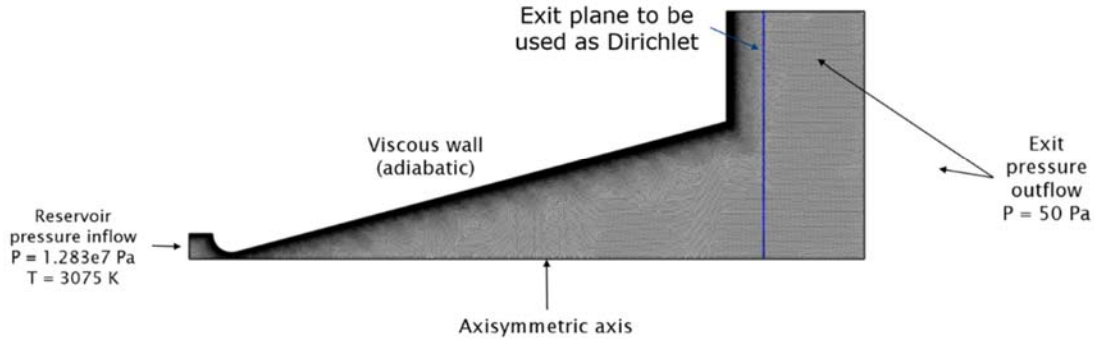


**Fig. 11:** Nozzle Simulation Numerical Set-up.

Fig. 12 shows a comparison between the Mach number distribution along the nozzle considering air as ideal gas and in thermal equilibrium and also for different turbulence modelling. Fig. 13 shows the Mach number, pressure and temperature variation according to axial distance and at the exit according to radial distance. Turbulence modelling does not affect the core flow but only in the wall region while the gas model affects the overall flow properties. The temperature is high enough not to be considered as ideal gas.

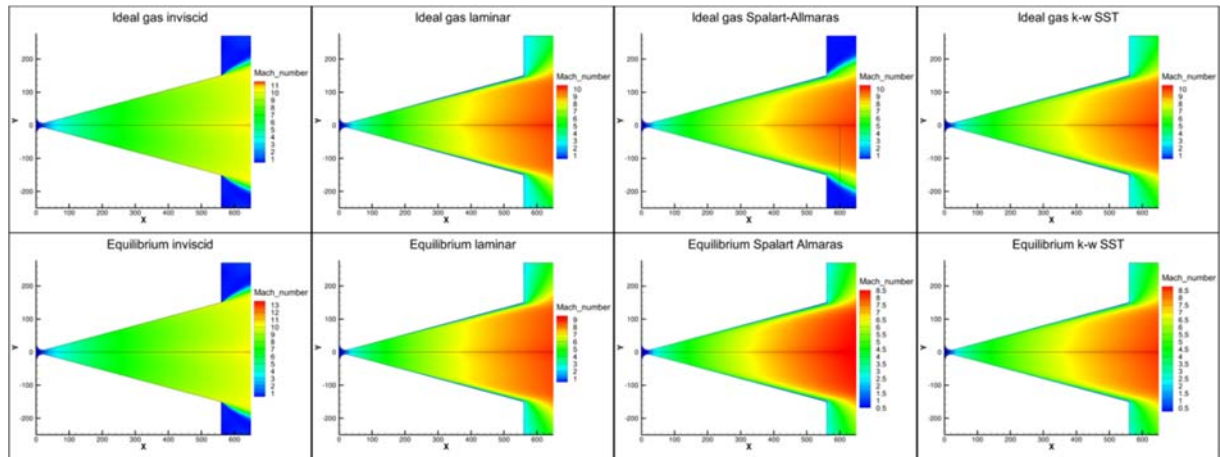


**Fig. 12:** Mach number contours pending on the boundary layer and gas state.

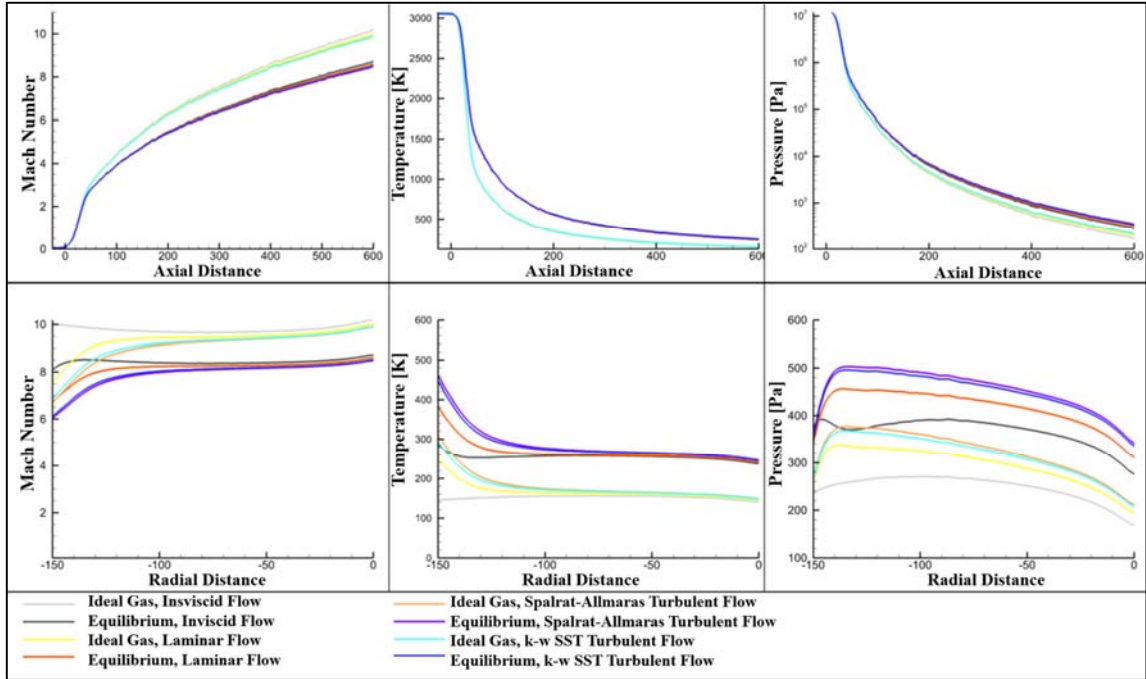


Fig. 13: Mach number, temperature and pressure pending on the boundary layer and gas state.

### 4.3. Conical Flow Divergence Effects Evaluation

To evaluate the conical divergence in the T2 nozzle, a slice 50 mm after the nozzle exit was extracted and utilized as inlet condition for the simulation of the experimental model. From the same slice the average core flow properties were extracted and used as farfield conditions for the experimental model simulation to compare only divergence effects for the same freestream flow properties.

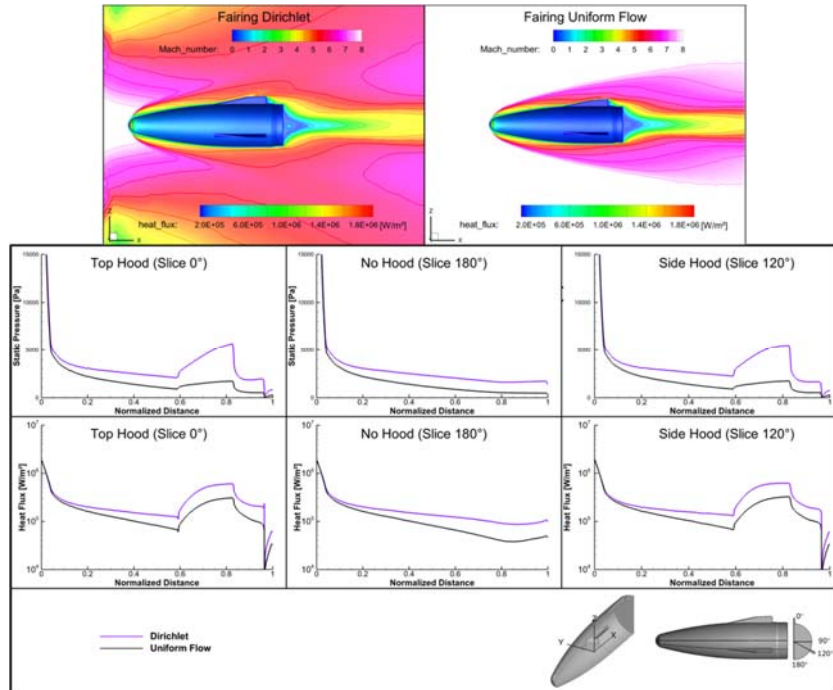
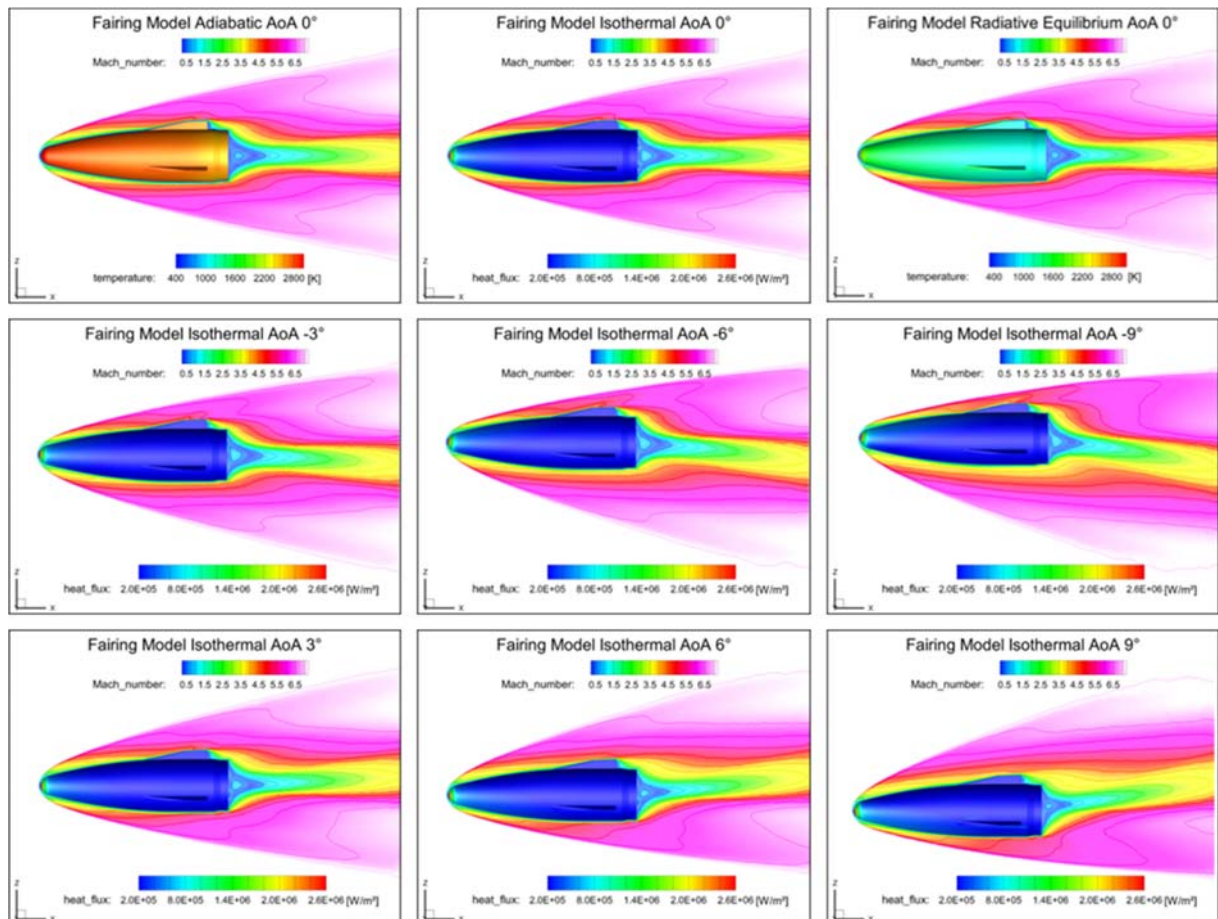


Fig. 14: Mach number and heat flux contour comparison between the Dirichlet and uniform flow.

**Fig. 14** shows the Mach number and heat flux contour comparison between the Dirichlet and uniform flow. Also, static pressure and heat flux plots over surface slices is shown for comparison and the flow divergence does not affect the stagnation point but the effects are representative along the model.

#### 4.4. Experimental Model Simulation

Based on the validated numerical set-up, the same mesh generation methodology and solver conditions were applied to simulate the experimental wind tunnel model including the hoods. This allowed comparing the blunted cone and the experimental model. To compose the aerothermodynamic database, CFD simulations at the determined tunnel conditions were carried out for the experimental model varying the angle of attack between  $-9.0^\circ$  and  $9.0^\circ$  and for various thermal boundary conditions at the wall to compare with simulations for the blunted cone. An adiabatic wall represents the most conservative in terms of wall temperature while a radiative equilibrium wall is more representative of a continuous cruise flight. For a booster trajectory, the short duration and the heating up of the fairing would definitely result in lower values. Fig. 15 shows a comparison between Mach number, heat flux and temperature contour between different wall conditions and angle of attack. As expected the adiabatic conditions are the worst-case scenario in terms of wall temperature while isothermal is the best case scenario to assess convective heat transfer. Due to the short duration of the test, the model wall will not heat up enough for the radiation to be significant, and hence the radiative equilibrium boundary condition is only representative for long duration testing.



**Fig. 15:** Comparison between Mach number contours and wall heat flux/temperature maps for experimental model simulations.

Fig. 16 shows the evolution of pressure coefficient, heat flux and temperature on the experimental model surface along different slices. They are taken at different conditions, i.e. adiabatic, radiative

equilibrium and isothermal cold wall, while varying the angle of attack between  $-9.00^\circ$  and  $9.00^\circ$ . As expected the boundary wall conditions have an effect on either the heat flux or temperature but not on the pressure coefficient. Since the model is symmetric, the AoA effects are symmetric despite the presence of hoods. The hoods have only a local effect and generate peaks in heat flux and pressure due to shock wave generation. This transient analysis is discussed in more depth in [11].

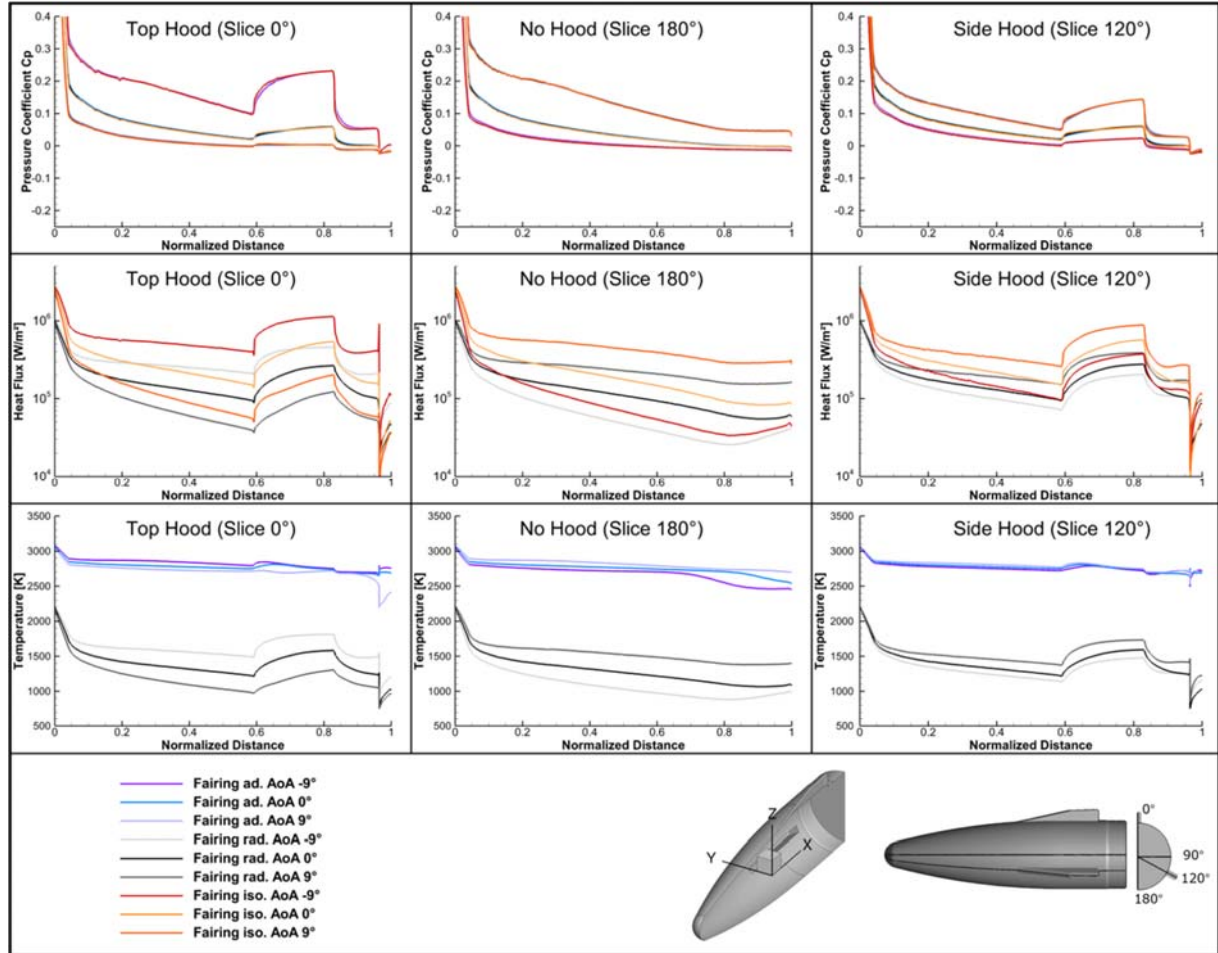


**Fig. 16:** Flow properties plots comparison between surface slices of experimental model.

#### 4.5. Wall conditions effects over the hoods

Protuberances in hypersonic flow generates shock waves leading to peaks of pressure and heat flux. Therefore, higher loads are expected on the hoods. An analysis of the wall temperature was made considering both adiabatic and radiative equilibrium considering angle of attack and is shown in Fig. 17. This type of analysis is not appropriate to select the hoods' material as it provides too high temperatures due to the nature of steady state simulation which is not the case during ascent. Therefore, as mentioned before, the sounding rocket passes quickly through the atmosphere and the wall temperature does not reach a steady state. A transient thermal analysis based on the wall heat flux along the trajectory is necessary for accurate estimation of wall temperature and hence the definition of the material and its thickness (see [11]).

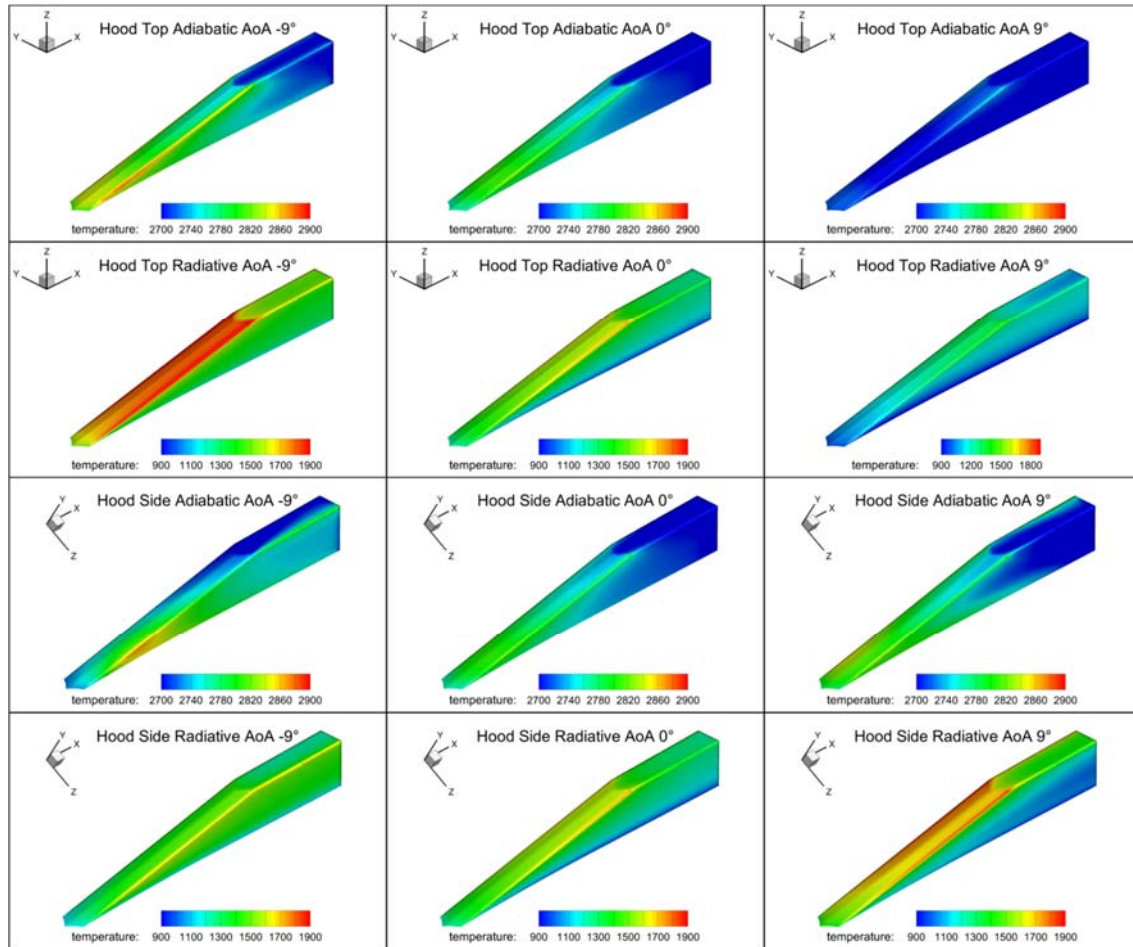


**Fig. 17:** Temperature distribution over the side hood for adiabatic and radiative equilibrium considering AoA.

## 5. Comparison between Experimental Results and CFD

### 5.1. Pressure Distribution

The steady freestream period was inferred from the plateau duration of the reservoir pressure to pitot probe ratio trace, as shown in Fig. 18. Thus, the temporal mean of the stagnation pressure, the freestream conditions and surface pressure measured by each sensor on the HXI fairing model could be determined. **Fig. 19** shows the experimental pressure distribution over the HXI fairing against AoA for slice  $0^\circ$  (blue colour), slice  $180^\circ$  (red colour) and near the hood (black colour). Each experimental point shown corresponds to an averaged pressure value normalized by the average total pressure of the shock layer close to the HXI fairing nose, considering of course the same freestream conditions and a given AoA. Overall, the data of the surface pressure distributions on the HXI fairing model for a given AoA confirm almost the same trends predicted by normalized CFD curves for whatever slice ( $0^\circ$ , close to  $0^\circ$  or  $180^\circ$ ). I.e. wall pressure decreases gradually and then peaks around the hood before decreasing again. Also, both experimental and CFD pressure distributions behave in a similar way as AoA changes. For slice  $0^\circ$ , the pressure around the hood becomes higher for more negative values of AoA and vice-versa (see **Fig. 13**)

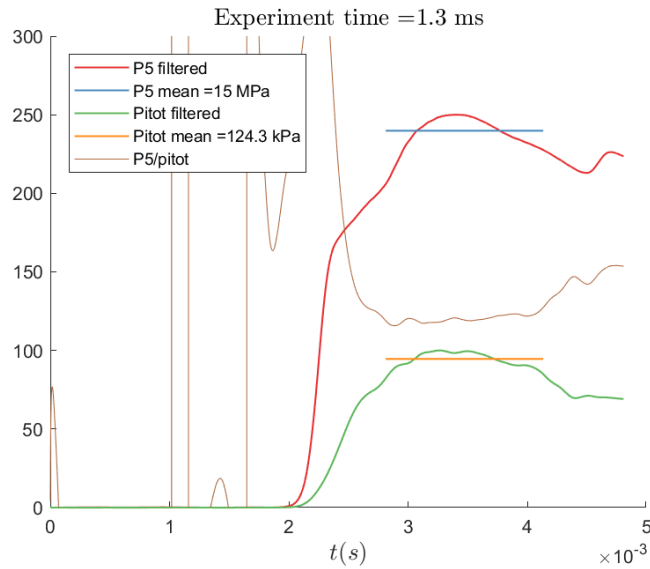
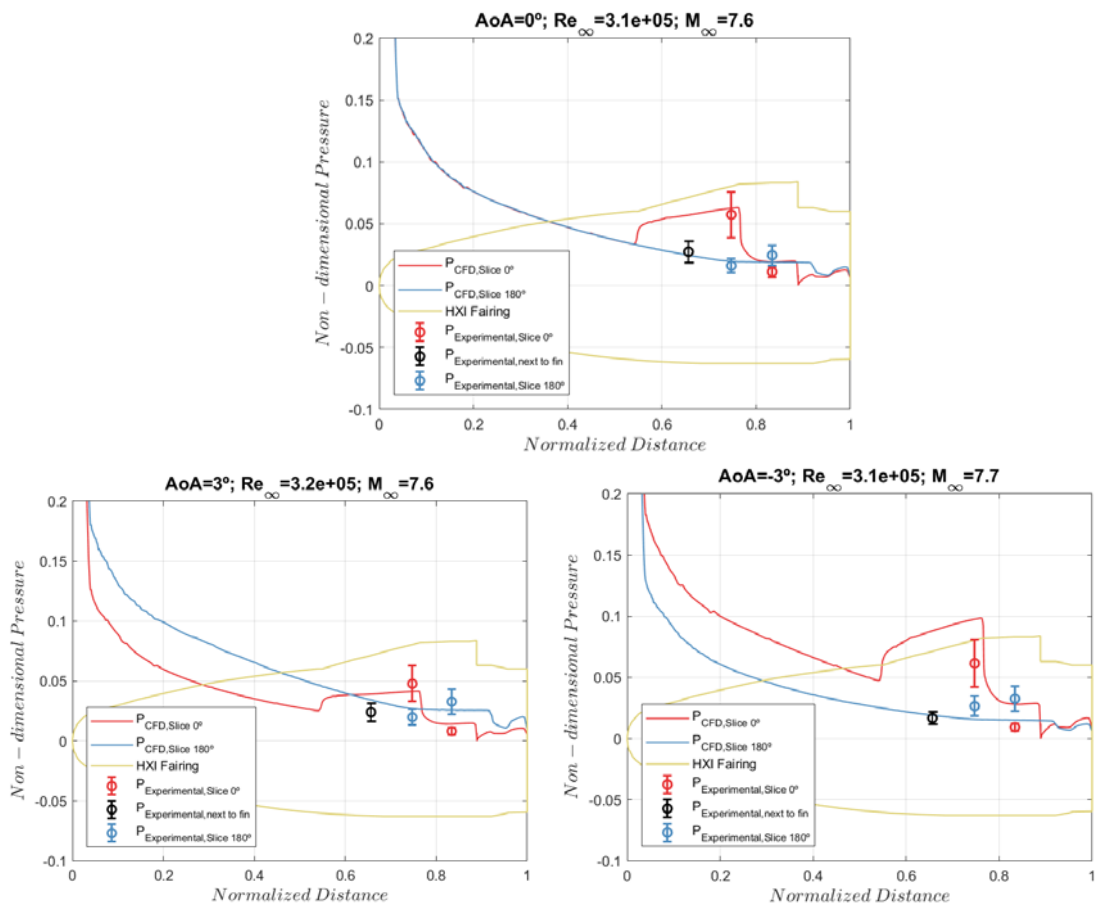
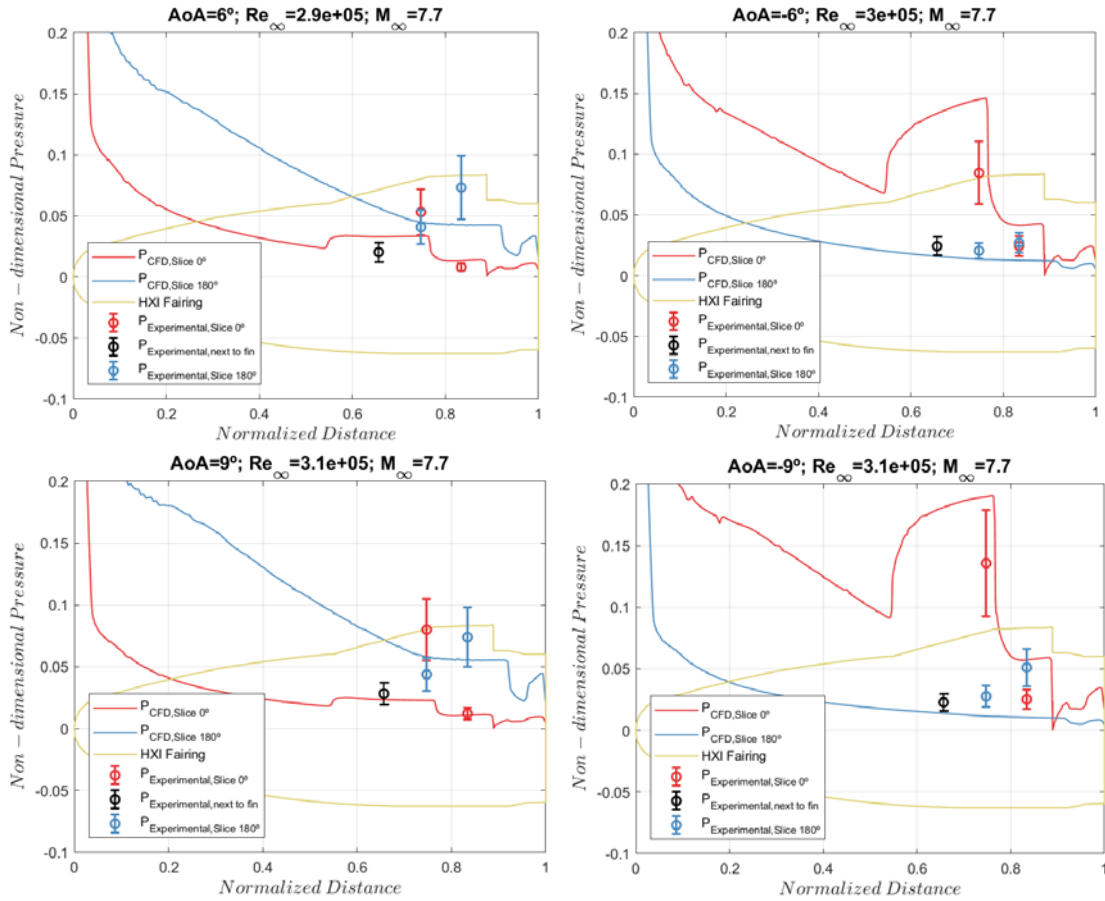


Fig. 18: Stagnation pressure and Pitot probe traces, showing their means over the plateau duration.





**Fig. 19:** Comparison between experimental and computational results for pressure distribution against AoA ranging from -9° to +9°. Results normalized by shock layer total pressure.

### 5.2. Flowfield Visualization and Stand-off Distance

For the visualization of the flowfield on the HXI sub-scaled fairing in the T2 test section during the test time, a high-speed “z-type” schlieren set-up was employed. **Fig. 20** illustrates the schlieren set-up, consisting basically of four mirrors with 203 mm of diameter, two concaves with a focal length of 1600 mm and two planes, a LED light source, a space filter (“knife”) and a DIMAX/PCO high-speed camera.

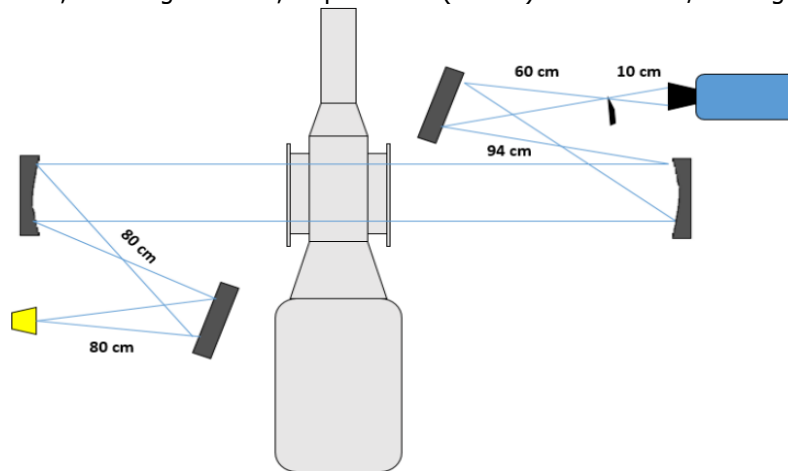


**Fig. 20:** Schematic diagram of the “z-type” schlieren technique of visualization.

A total of 32 visualizations were done: 21 of them dedicated to visualize the flowfield in front of the HXI fairing model and the rest of them visualizing the characteristics of the flow around the hood (0° slice). From schlieren images shown in **Fig. 21**, it is possible to state that, over the test time during which the freestream is steady, whatever the angle of attack within -9 and +9 degrees, there is no strong interaction of the bow shock wave observed with the hoods. Also, it seems that the hoods do not induce any shock wave. Both facts were also predicted by CFD simulations, as observed from contours plots in Fig. 12. Also, based on such schlieren images, it was possible to determine the stand-off distance ( $\delta$ ) of the bow shock wave in front of the HXI fairing and its relation with AoA (see subsection 6.1). Fig. 22 shows the flowfield features around the HXI fairing nose at hypervelocity during the test time of run #5. Orange colour may correspond to the radiative emission of hot gas from shock layer in front of HXI nose and around 120°-slice hood.

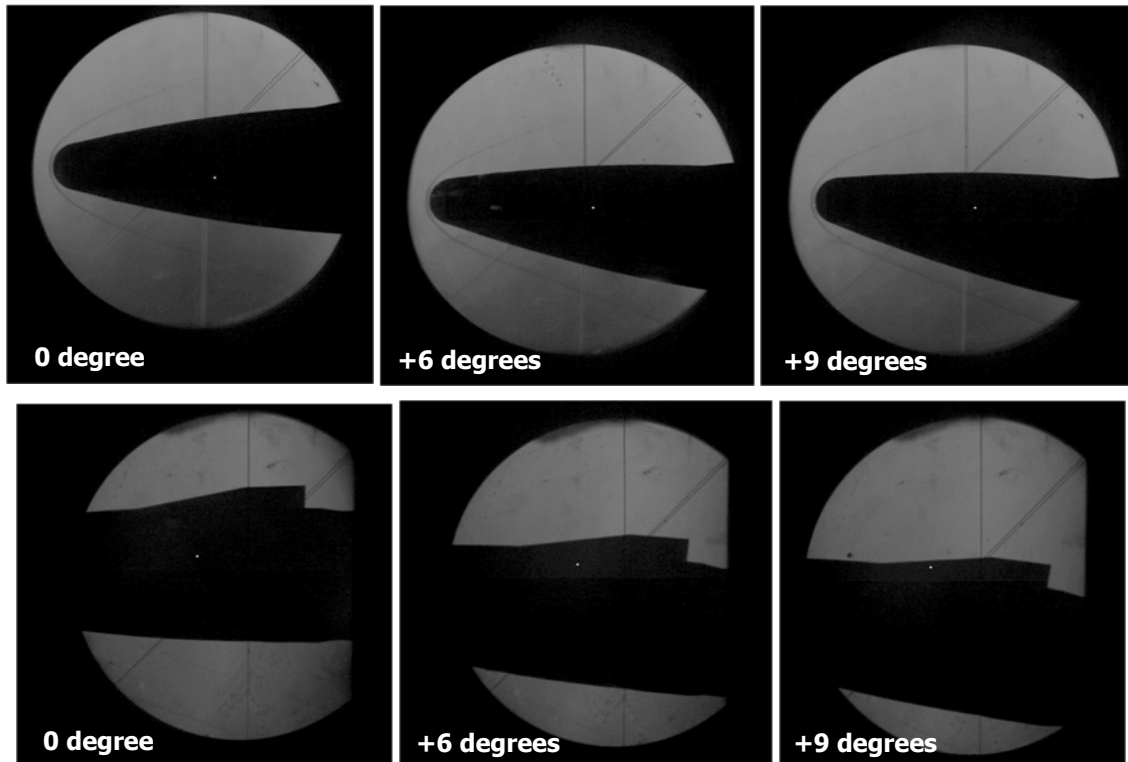


**Fig. 21:** Schlieren images for AoA ranging from 0° to +9°, showing the flowfield around HXI fairing nose (top) and close to the 0°-slice hood (bottom).

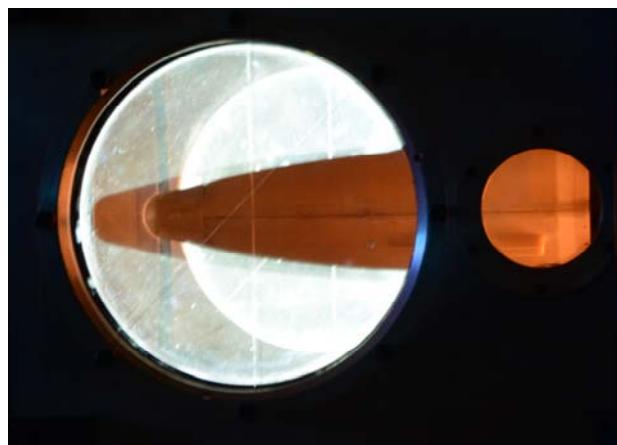


**Fig. 22:** Picture (bulb mode) of the sub-scale model of HXI fairing in T2 test section during run#5 (freestream Mach number 7.8 and Reynolds number 3.4E+05).

Fig. 23 shows the stand-off distance ( $\delta$ ) of the bow shock from the stagnation point of the HXI fairing against AoA. Note that the stand-off distance seems to be independent of AoA as revealed by experimental data (from visual inspection of schlieren images shown in subsection 6.2) and CFD predictions (from visual inspection of Mach number contours in **Fig. 15**). Also, calculations based on an approximate expression for stand-off distance [12] given by equation (4), in the limit of high velocities, results in  $\delta$  of around 2.5 mm, which lies in between experimental and CFD values of stand-off distance:

$$\frac{\delta}{R} \cong \frac{1}{\left(\frac{\rho_2}{\rho_1}\right)} \quad (4)$$

where  $R = 13.89$  mm is the radius of curvature of the HXI sub-scaled fairing nose,  $\rho_1$  and  $\rho_2$  are the calculated density upstream and downstream of the normal portion of the bow shock.

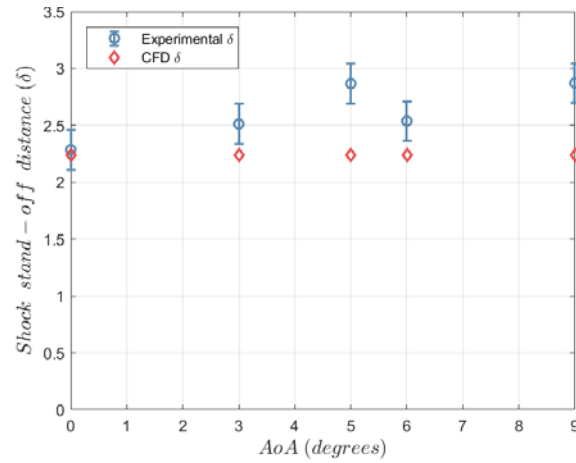


**Fig. 23:** Comparison between experimental data and computational prediction for stand-off distance (in mm) against AoA ranging from  $0^\circ$  to  $+9^\circ$ .

## 6. Extrapolation to Flight

### 6.1. Scale Verification

The first set of simulation were performed to compare the CFD results with theoretical ones considering a blunted cone. Considering that the numerical set-up is validated, an aerothermodynamics database was built for the experimental model for further experimental validation. Since the final purpose of this work is to extrapolate and to generate an aerothermodynamics database for the real flight model, it is necessary to check the scaling as well. **Fig. 24** gives a comparison of between the CFD simulations for the real full-scale fairing and the experimental model at those flow properties respecting Mach and Reynolds similarity ( $\rho L$  scaling). The results are similar for both validating the scaling utilized.

### 6.2. Flight Fairing Aerodynamic Database

For the preliminary design of the flight fairing, a complete aerothermodynamic analysis along the trajectory is necessary to determine the load applied to it. Based on the presented mission profile (VBS43 trajectory), points along the trajectory were extracted for numerical analysis (Fig. 7). Table 2 presents the extracted points used in the aerothermal database to evaluate the highest loads at transonic speed and highest dynamic pressure. Same meshing and solver setting were used in the numerical set-up.

Atmosphere composition changes substantially according to altitude and the air becomes less dense with lower pressure. The first fourteen critical points along the trajectory are below 40 km, at altitudes higher than 40 km the loads will be lower. However, since the vehicle spends half of its trajectory between 40 and 75 km, four points along the trajectory were chosen to evaluate the aerothermodynamics loads accurately. **Fig. 24** shows a Mach number contour comparison of the flowfield around the flight fairing and wall heat flux map on the model surfaces along the trajectory.

Pressure and heat flux become lower with altitude for similar Mach number. **Fig. 26** shows also a comparison between pressure coefficient, heat flux and heat flux coefficient distribution through surface slices in the fairing flight model according to the trajectory. As expected, the loads become more intense with Mach number and then decrease with altitude.

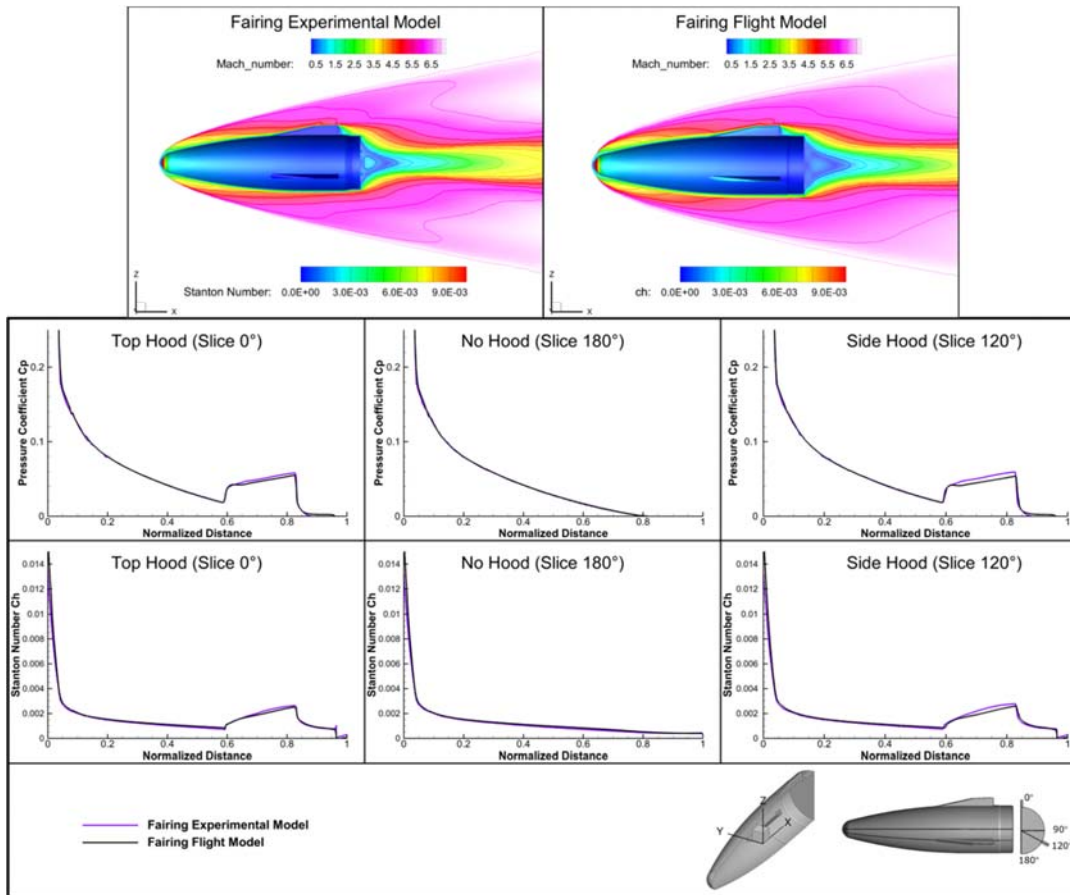


**Fig. 24:** Shock tunnel and flight model CFD comparison.

**Table 2 - Critical aero-thermal load points along the flight path for numerical analysis**

Point	Time [s]	Altitude [km]	Mach Number	Dyn. Pressure [Pa]	Atm. Pressure [Pa]	Atm. Temp. [K]	Total AoA [°]	Atm. Density [kg/m <sup>3</sup> ]	Reynolds Number [1/m]
1	6.5	0.36	0.29	5.99E+03	9.71E+04	286	3.44	1.18E+00	6.60E+06
2	15.0	1.85	0.80	3.65E+04	8.10E+04	276	6.41	1.02E+00	1.56E+07
3	16.5	2.23	0.91	4.50E+04	7.72E+04	274	6.02	9.83E-01	1.71E+07
4	17.0	2.37	0.95	4.81E+04	7.60E+04	273	5.88	9.70E-01	1.76E+07
5	18.0	2.64	1.03	5.45E+04	7.33E+04	271	5.55	9.43E-01	1.86E+07
6	19.0	2.93	1.11	6.16E+04	7.07E+04	269	5.13	9.15E-01	1.96E+07
7	20.0	3.23	1.21	6.92E+04	6.81E+04	267	4.69	8.88E-01	2.35E+07
8	29.0	6.29	2.03	1.32E+05	4.53E+04	247	0.06	6.39E-01	2.57E+07
9	36.5	9.60	2.99	1.77E+05	2.82E+04	226	0.04	4.34E-01	2.64E+07
10	40.0	11.42	3.56	1.89E+05	2.12E+04	217	0.03	3.42E-01	2.51E+07
11	43.0	13.15	4.04	1.86E+05	1.62E+04	217	0.03	2.61E-01	2.17E+07
12	52.5	19.80	6.00	1.44E+05	5.71E+03	217	0.02	9.18E-02	1.14E+07
13	56.5	23.26	7.02	1.15E+05	3.33E+03	220	0.02	5.28E-02	7.60E+06
14	60.0	26.69	8.02	8.89E+04	1.97E+03	223	0.03	3.08E-02	5.04E+06
15	75.0	41.65	7.47	9.02E+03	2.30E+02	255	0.02	3.15E-03	4.59E+05
16	90.0	54.48	7.19	1.64E+03	4.55E+01	262	0.02	6.04E-04	8.39E+04
17	105.0	65.28	7.47	4.10E+02	1.05E+01	233	0.03	1.57E-04	2.36E+04
18	122.0	75.11	7.76	9.90E+01	2.40E+00	208	0.01	3.92E-05	6.36E+03

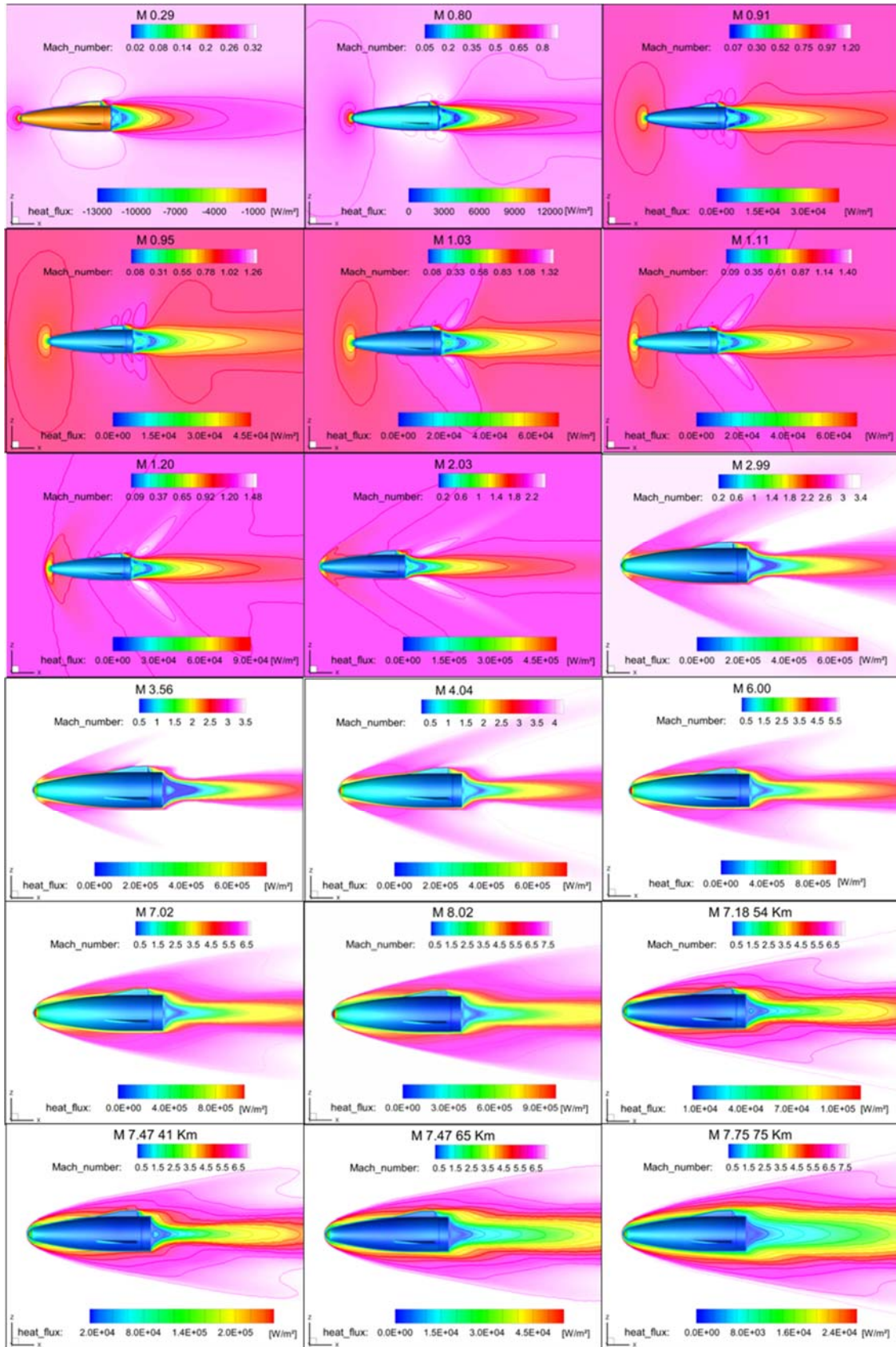


**Fig. 25:** Comparison between Mach number contours and wall heat flux according to trajectory.

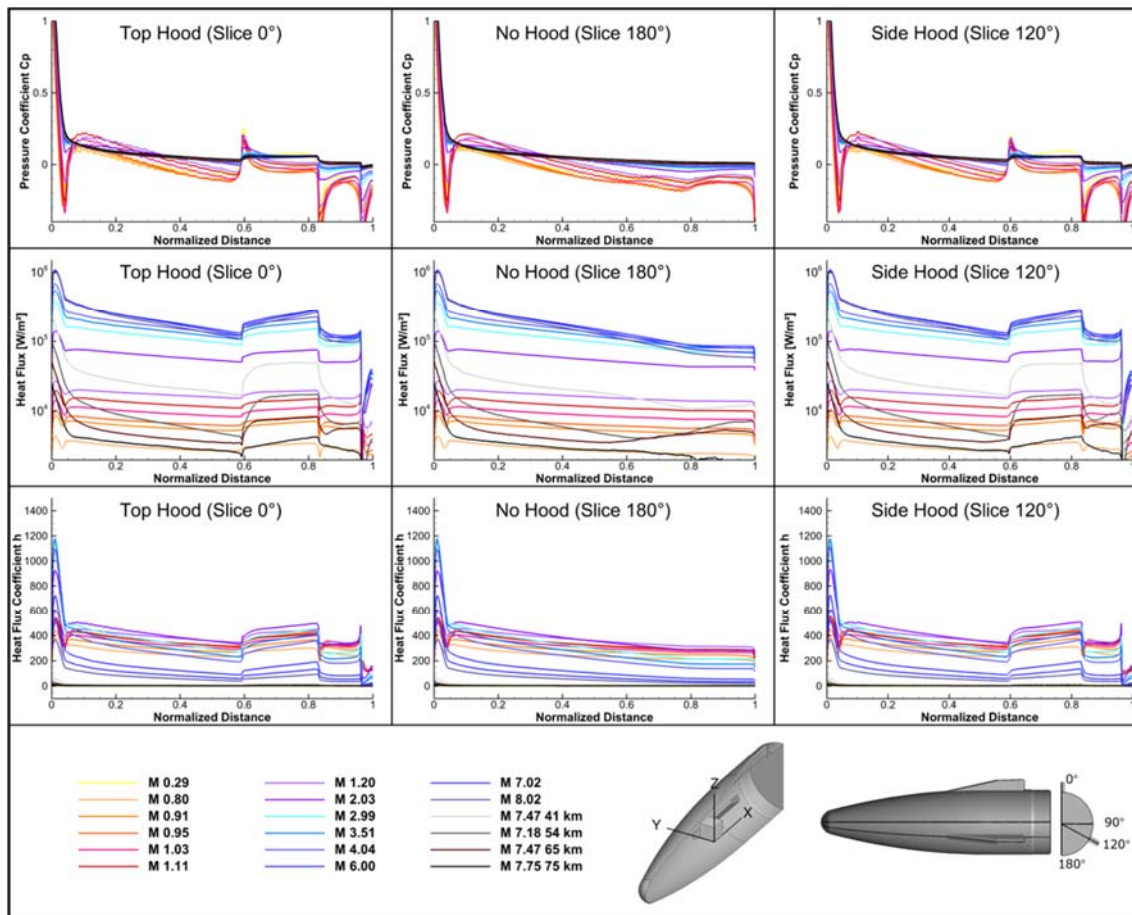


**Fig. 26:** Pressure and heat flux plots between surface slices according to trajectory.

## 7. Final considerations

The present paper dealt with the aerodynamic performance analysis of a hooded fairing. Based on the mission scenario of HXI for the VS43 ascent trajectory, different flight segments were numerically analysed. This will allow the aero-thermal loads determination needed for the fairing design and manufacture. In the final paper, experimental results shall validate the compliance of CFD simulation with respect to hooded fairing aerodynamic performance.

## Acknowledgements

This work was performed within the 'High Speed Experimental Fly Vehicles - International' project fostering International Cooperation on Civil High-Speed Air Transport Research. HEXAFly-INT, coordinated by ESA-ESTEC, is supported by the EU within the 7th Framework Programme Theme 7 Transport, Contract no.: ACP3-GA-2014-620327 and by the Ministry of Industry and Trade, Russian Federation. Further info on HEXAFly-INT to be found on [http://www.esa.int/techresources/hexafly\\_int](http://www.esa.int/techresources/hexafly_int).

The first author would like to thank ESA for receipt of the International Research Fellowship in the framework of international collaboration between ESA and Brazil.

## References

1. Bertin, J. J., Cummings, R. M.: Fifty Years of Hypersonics: Where We've Been, Where We're Going, Progress in Aerospace Sciences, v. 39, 511-536, 2003
2. Steelant, J., Langener, T., Hannemann, K., Riehmer, J., Kuhn, M., Dittert, C., Jung, W., Marini, M., Pezzella, G., Cicala, M., Serre, L.: Conceptual Design of the High-Speed Propelled Experimental Flight Test Vehicle HEXAFly. In: 20th AIAA International Space Planes and Hypersonic Systems and Technologies Conference, 5-8 July, Glasgow, Scotland, AIAA-2015-3539, (2015)
3. Menezes, A.C., Rosa, M.A.P., Rocamora Jr., F.D., Assenção, J.A.S., Galvão, V. A. B.: Valuation of the Operational Performance Maps for the IEAV's Hypersonic Tunnel T2. IN: 21st Brazilian Congress of Mechanical Engineering October 24-28, Natal, RN, Brazil, (2012)
4. Rego, I.S. et al., Ground experimentation with 3-D printed scramjet inlet models at hypervelocities. Aerospace Science and Technology, v. 55, p. 307-313, ISSN 1270-9638, (2016).
5. Wada, Y., Liou, M.S., "A flux splitting scheme with high-resolution and robustness for discontinuities", AIAA Paper 94-0083, 1994.
6. Institute of Aerodynamics and Flow Technology, German Aerospace Center (DLR), The DLR TAU Code, 2012. url: <http://tau.dlr.de/>.
7. Spalart, P.R., Allmaras, S.R., "A One-Equation Turbulence Model for Aerodynamic Flows", AIAA-92-0439, 1992.
8. Anderson, W. Kyle, Bonhaus, Daryl L., "An Implicit Upwind Algorithm for Computing Turbulent Flows on Unstructured Grids". Computers and Fluids, Vol. 23, No. 1, pp. 1-21, 1994.
9. Haselbacher, A., Blazek, J., "Accurate and Efficient Discretization of the Navier-Stokes Equations on Mixed Grids", AIAA Journal, Vol. 38, No. 11, pp. 2094-2102, November 2000.
10. White, F. M., "Viscous Fluid Flow". New York: McGraw-Hill, 2nd edition, 1974.
11. Van den Eynde J., Martos J.F.A., Jasko A., Appolloni M., Steelant J., Kallenbach A., Shardin A., Gorskiy A., 'Preliminary Design of a Hooded Fairing Accommodating Winged Payloads', Int. Conference on High-Speed Vehicle Science Technology (HiSST), 26-29 November 2018, Moscow, Russia
12. Anderson, J. D., Hypersonic and High Temperature Gas Dynamics, AIAA, 1<sup>st</sup> edition, 513-514, 1989.
13. Minucci, M. A. S., An Experimental Investigation of a 2-D Scramjet Inlet at Flow Mach Numbers of 8 to 25 and Stagnation Temperatures of 800 to 4,100 K, PhD thesis, Rensselaer Polytechnic Institute, Troy, 1991.